Nanoscale Advances

ROYAL SOCIETY OF CHEMISTRY

PAPER

View Article Online
View Journal | View Issue

Cite this: *Nanoscale Adv.*, 2023, **5**, 6925

Squeezed Darcy–Forchheimer Casson nanofluid flow between horizontal plates under the effect of inclined magnetic field

M. Asif Memon, [a] Dur-e-Shehwar Sagheer,[b] Mushrifah A. S. Al-Malki,[c] Muhammad Sabeel Khan,[b] Shafqat Hussain,[d] Haseeb ur Rehman[b] and Amsalu Fenta *[e]

This article explores the properties of heat and mass transport for MHD Casson nanofluid flow between two horizontal plates by considering the Darcy–Forchheimer medium. The effects of a uniform inclined magnetic field are discussed numerically. A Darcy–Forchheimer medium is considered in the x-direction between two plates. The features of Brownian diffusive motion, porosity, friction, viscous dissipation, chemical reaction, and thermophoresis are also considered. The governing equations of the model are a system of partial differential equations. This system is converted into non-linear ordinary differential equations using suitable similarity functions. The numerical shooting technique is used to solve the attained boundary value problem. This numerical technique is endowed with the Runge–Kutta order four method and the Newton method. Graphs and tables depict different significant effects. It is observed that the effect of a magnetic field is inversely related to the fluid flow. Moreover, the porosity factor (λ) and the magnetic inclination (γ) are inversely related to the surface drag force (C_f) and the Nusselt number (N_u).

Received 12th September 2023
Accepted 10th October 2023

DOI: 10.1039/d3na00769c

rsc.li/nanoscale-advances

1 Introduction

Physical scenarios containing viscous fluid involve the natural phenomenon of heat and mass convection. This phenomenon occurs naturally in many formations, including two parallel plates, stretched surfaces, and inside cylinders and spheres. The phenomenon of fluid moving between two surfaces is called squeezing flow. Researchers who investigated fluid flow, heat, and mass transport have given significant attention to squeezing flow because of its importance and applications in industry. Furthermore, in the last decade, many classical hydrodynamics flow problems obtained new consideration within the more general context of hydrodynamics. Many fields, such as chemical, mechanical, and biochemical engineering, food, and industrial processing, are emblematic examples of areas involving squeezing flow. Additionally, many applications can be seen in automobiles, lubricants, rolling elements, machine devices, and gears.

Investigations have[1–4] provided excellent information on steady, laminar, incompressible, free convection boundary-layer flow down a vertical plate immersed in a thermally stratified fluid-saturated porous media in the presence of a uniform normal magnetic field. The growing laminar free convection of a micro-polar fluid in a vertical parallel plate channel with asymmetric heating is addressed numerically and analytically in ref. 5. The squeezing flow is first discussed by Stefan,[6] which is well regarded by the scientific community with helpful remarks on the different profiles of fluid flow. After that, the squeezing flow was extensively addressed by many researchers. Rashidi *et al.*[7] discussed the unsteady axisymmetric and 2D squeezing flows lying between two parallel plates. These authors found the solutions analytically by HAM and validated the effects of the squeezing parameter on skin friction and Nusselt number using the fourth-order Runge–Kutta method. In 2015, Hayat *et al.*[8] revealed the different properties of 3D squeezing flow between two sheets using mixed convection. They found that with the rotation increase, the suction parameters are directly related to the magnitude of the drag force coefficient and the local Nusselt number. In another study, Hayat *et al.*[9] demonstrated a flow in a rotating channel squeezed between two disks and discovered that the velocity profile increases with an enhancement in the squeezing parameter. Shahmohamadi and Rashidi[10] reported some attractive verdicts on squeezing nano-fluid flow within a rotating channel where the lower plate is

[a]*Department of Mathematics and Social Sciences, Sukkur IBA University, Sukkur, 65200, Sindh, Pakistan. E-mail: asif-memon@iba-suk.edu.pk*

[b]*Department of Mathematics, Capital University of Science and Technology, 44000 Islamabad, Pakistan. E-mail: d.e.shehwar@cust.edu.pk; muhammad.sabeel@cust.edu.pk; haseebchohan165@gmail.com*

[c]*Department of Mathematics and Statistics, College of Science, Taif University, P. O. Box 11099, Taif 21944, Saudi Arabia. E-mail: m.malky@tu.edu.sa*

[d]*Department of Mathematics, LS-III, Technical University Dortmund, Germany. E-mail: shafqat.hussain@math.tu-dortmund.de*

[e]*Department of Physics, Mizan Tepi University, PO Box 121, Tepi, Ethiopia. E-mail: amsalu.fenta09@gmail.com*

porous. The obtained consequences showed that an increase of nanoparticles significantly affects the shear stress near the walls and the velocity profiles of the flow. Some recent studies[11–13] are referred to for better understanding of the flows mentioned above. Nanofluids have more practical features[14–16] in fluid mechanics due to technological advancements since the thermal properties of the nanofluid are better (see for instance ref. 17) than those of the fluids. These fluids have metallic nanoparticles dispersed in the base fluid. Nanofluids have provided considerable advances due to their thermal properties and dynamic suppleness in terms of irreversibility, entropy, and many other relevant features. The pioneering study in this area was conducted by Choi,[18] illustrating nanoparticle effects on the underlying liquid's thermo-physical properties. The research community appraised the idea practically by considering nanofluids in different flow problems. Later, Parvin and Chamkha[19] analyzed nanofluid flow with entropy generation and free convection in an odd-shaped cavity. Zaraki *et al.*[20] disclosed the convection properties within the boundary layer by considering additional properties of nanoparticles, *e.g.*, size, type, and shape. Reddy and Chamkha[21] accounted for the flow, heat, and mass transfer of MHD viscous, incompressible nanofluid flow with heat absorption/generation upon a homogeneously stretching sheet. Flow is considered in a porous medium with thermal radiation, chemical reaction, and thermal diffusion effects. Results of this article reveal that the increase in Rayleigh number is a reason for an increment in the average Nusselt number and the heat transport of entropy generation but a decrease in the viscous term. Chamkha *et al.*[22] studied the entropy optimization and impact of magnetic parameters in a water-based nanofluid. Rasool *et al.*[23] discussed the impacts of the porous medium on nanofluid flow over an expanding surface and demonstrated that skin friction increases significantly due to the porous medium, because of the high resistance of porosity. The heat and mass flux is decreased for a stronger porosity factor. This observation is crucial for industries where nanofluids are used. Ismael *et al.*[24] analyzed nanofluid flow in a cavity filled with a porous media and studied entropy optimization. Many recent articles[25–29] are focused on the analysis of the flow of nanofluids. Recently, Murtaza *et al.*[11] addressed how the improved thermophysical properties of nanofluids have a substantial impact on how successful they are in convection processes. A few interesting studies on hybrid nanofluids can be found in the literature.[15,30]

The laws of Darcy are widely used to model and analyze the flows with fluid in a porous medium. If the Reynolds number is greater than one, then extra hydrodynamic head loss occurs due to inertial effects, making the flow non-Darcian. Forchheimer[31] sum up the effects of inertia by introducing a non-linear term on the reduction of apparent permeability. This development is termed the Darcy–Forchheimer model. Muskat and Wyckoff[32] presented homogeneous fluid flow through the Darcy medium. This classical study presents an analytical solution to the problem of combined seepage under a sheet piling cofferdam applied to dewatering systems. Seddeek[33] considered the flow incorporating mixed convection to study the impacts of thermophoresis and viscous dissipation in Darcy-type fluid flow. The authors discovered that in this scenario, an increase in the thermophoretic parameter decreases the velocity and increases the boundary layer. Sadiq and Hayat[34] considered Maxwell liquid to report the 2D, MHD flows over a surface expanding with linear velocity. Their findings reveal that the temperature profile is inversely associated with the thermal relaxation parameter and Prandtl number. Hayat *et al.*[35] conducted a study of Darcy-type nanofluid flow with chemical reaction and heat generation. Rasool *et al.*[36] considered a nanofluid flow in a Darcy–Forchheimer medium between two horizontal plates under the effect of a uniform magnetic field. The findings of this article reveal that the thermal profile decreases for increasing viscosity parameters; moreover, Brownian diffusion and thermophoresis increase for the said profile. An increase is observed in surface drag force for the elevated values of the porosity parameter.

This study presents an investigation of the inclined magnetic field on the Forchheimer porous Casson flow between horizontal plates. It extends the problem highlighted in ref. 36 by providing a numerical analysis of magneto-hydrodynamic Casson flow with porosity under the inclined magnetic field effects. The interaction of an inclined magnetic field in porous medium between plates can have different interesting applications, for instance, inclined magnetic fields can be utilized for improved efficiency in oil and gas reservoirs; in removal of contaminants from groundwater in aquifers; in heat exchangers and cooling systems, in measuring the magnetic response of porous formations; in electromagnetic braking in pipes; in filtration and separation processes and in microfluidic systems. From the primitive years, mass transfer has played an essential role in understanding the ocean's vaporization, burning of oil pools, spray drying, leaching, and the abolition of a meteorite. Due to this critical role of mass transfer, we also considered the concentration equation in the flow model.

2 Mathematical modeling

Consider a steady Casson fluid flow squeezed between two plates separated by distance h and adjusted horizontally. The lower plate is fixed at $x_2 = 0$ and the upper plate at $x_2 = h$ Cartesian coordinates. The lower plate is stretching with velocity $u_1 = \varpi x_1$, where ϖ is a positive integer. A magnetic field inclined at an angle γ with the horizontal x_1-axis is considered to act uniformly in the flow. The flow is along the horizontal axis between the plates in the Darcy–Forchheimer medium with the additional effects of porosity and viscous dissipation. Moreover, the flow concentration is discussed using a concentration equation during a chemical reaction. The geometrical scenario of the flow problem is represented in Fig. 1.

The governing equations for mass, momentum, energy, and concentration conservation in the presence of viscous dissipation, chemical reaction, thermophoretic motion and Brownian motion constitute the following mathematical model governing the flow (see ref. 37):

Equation of continuity:

$$\nabla \cdot V = 0 \tag{1}$$

Equation of momentum:

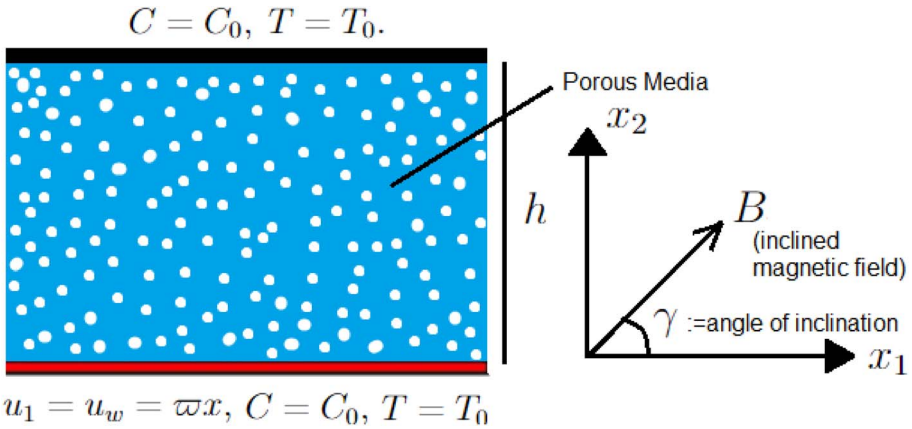

Fig. 1 Geometric framework of the problem through porous flow.

$$\rho(V\cdot\nabla)V = -\nabla p + \rho g + \mu\nabla^2 V - \frac{\mu}{K}V + H \tag{2}$$

Energy equation:

$$\rho C_p(V\cdot\nabla)T = \alpha\nabla^2 T + \alpha\left[\left(\frac{\partial u}{\partial x}\right)^2 + \left(\frac{\partial v}{\partial y}\right)^2\right] + \tau\left[D_b\nabla C\cdot\nabla T + D_T\frac{\nabla T\cdot\nabla T}{T}\right] + \frac{\nu_f}{C_p}\left(\frac{du_1}{dx_2}\right)^2 \tag{3}$$

Concentration equation:

$$(V\cdot\nabla)C + K_c(C - C_h) = D_b\nabla^2 C. \tag{4}$$

The term H in eqn (2) is the current density times the velocity vector. Ohm's law gives the form of the current density vector $J = \sigma(V \times B) = (0,\ 0,\ uB_0\sin\gamma - vB_0\cos\gamma)$, in which σ is the electrical conductivity, and $V = (u_1, u_2, 0)$ is the velocity vector. Hence, we obtain the Lorentz force:

$$J \times B = (\sigma {B_0}^2 u_2 \sin\gamma\cos\gamma - \sigma {B_0}^2 u_1 \sin^2\gamma,\ \sigma {B_0}^2 u_1 \sin\gamma\cos\gamma - \sigma {B_0}^2 u_2 \sin\gamma\cos^2\gamma, 0).$$

In the above model description, thermal equilibrium between the fluid and porous media has been assumed in the present study. This is because the concept is applicable to many engineering and scientific applications. For instance, thermal equilibrium between the fluid and porous media is assumed in geothermal reservoirs, underground heat exchangers, and in many studies dealing with heat transfer through porous media in the literature. The component parts of the model (eqn (1)–(4)), now read:

$$\frac{\partial u_1}{\partial x_1} + \frac{\partial u_2}{\partial x_2} = 0, \tag{5}$$

$$u_1\frac{\partial u_1}{\partial x_1} + u_2\frac{\partial u_1}{\partial x_2} = -\frac{1}{\rho_f}\frac{\partial p}{\partial x_1} + \nu\left(1+\frac{1}{\beta}\right)\left(\frac{\partial^2 u_1}{\partial x_1^2} + \frac{\partial^2 u_1}{\partial x_2^2}\right) - \frac{\nu}{K}\left(1+\frac{1}{\beta}\right)u_1 - Fu_1^2 + \frac{\sigma B_0^2}{\rho_f}\sin\gamma(u_2\cos\gamma - u_1\sin\gamma), \tag{6}$$

$$u_1\frac{\partial u_2}{\partial x_1} + u_2\frac{\partial u_2}{\partial x_2} = -\frac{1}{\rho_f}\frac{\partial p}{\partial x_2} + \nu\left(1+\frac{1}{\beta}\right)\left(\frac{\partial^2 u_2}{\partial x_1^2} + \frac{\partial^2 u_2}{\partial x_2^2}\right) + \frac{\sigma B_0^2}{\rho_f}\cos\gamma(u_1\sin\gamma - u_2\cos\gamma), \tag{7}$$

$$u_1\frac{\partial T}{\partial x_1} + u_2\frac{\partial T}{\partial x_2} = \alpha\left(\frac{\partial^2 T}{\partial {x_1}^2} + \frac{\partial^2 T}{\partial {x_2}^2}\right) + \tau\left[D_B\left(\frac{\partial C}{\partial x_2}\frac{\partial T}{\partial x_2} + \frac{\partial C}{\partial x_1}\frac{\partial T}{\partial x_1} + \frac{D_T}{T_h}\left(\frac{\partial T}{\partial x_1}\right)^2 + \left(\frac{\partial T}{\partial x_2}\right)^2\right)\right] + \frac{\nu_f}{C_p}\left(\frac{\partial u_1}{\partial x_2}\right)^2, \tag{8}$$

$$u_1\frac{\partial C}{\partial x_1} + u_2\frac{\partial C}{\partial x_2} + K_c(C - C_h) = D_B\left(\frac{\partial^2 C}{\partial x_1^2} + \frac{\partial^2 C}{\partial x_2^2}\right) + \frac{D_T}{T_h}\left(\frac{\partial^2 T}{\partial x_1^2} + \frac{\partial^2 T}{\partial x_2^2}\right). \tag{9}$$

The components of velocity along the x_1 and x_2 directions are denoted by u_1 and u_2, respectively. The following conditions are associated with the boundaries:[36,38]

$$\left.\begin{array}{l}\text{at } x_2 = 0, u_1 = u_w = \varpi x, C = C_0, T = T_0,\\ \text{at } x_2 = h, C = C_0, T = T_0.\end{array}\right\} \tag{10}$$

The following similarity transformation is used to convert partial differential equations eqn (5)–(10) into a boundary value problem:

$$u_1 = \varpi x_1\frac{\partial f}{\partial \eta}, u_2 = -\varpi h f,\ \theta(\eta) = \frac{T - T_h}{T_0 - T_h},\ \phi(\eta) = \frac{C - C_h}{C_0 - C_h}\Big\}. \tag{11}$$

As a consequence of eqn (11), the governing equations acquire the following non-dimensional forms:

$$\left(1+\frac{1}{\beta}\right)f^{(\mathrm{iv})} - P\left(f'f'' - ff'''\right) - \lambda\left(1+\frac{1}{\beta}\right)f'' \\ -2F_{\mathrm{r}}\left(f'\right)\left(f''\right) - \sin\gamma\left[\sin\gamma f'' - 2\delta\cos\gamma f'\right]M = 0, \tag{12}$$

$$\theta'' + N_{\mathrm{b}}\theta'\phi' + N_{\mathrm{t}}\theta'^2 + P_{\mathrm{r}}(Pf\theta' + E_{\mathrm{c}}f''^2) = 0, \tag{13}$$

$$\phi'' + PS_{\mathrm{c}}f\phi' + \frac{N_t}{N_{\mathrm{b}}}\theta'' - RS_{\mathrm{c}}\phi = 0. \tag{14}$$

The associated boundary conditions given in eqn (10) have the following dimensionless form:

$$\left.\begin{array}{llll} \text{at } \eta = 0 & f = 0, & f' = 1, & \theta = 1 = \phi, \\ \text{at } \eta = 1 & f = 0, & f' = 0, & \theta = 0 = \phi, \end{array}\right\} \tag{15}$$

where the viscosity parameter $P = \frac{h^2\varpi}{\nu}$, porosity $\lambda = \frac{h^2}{k}$, Forchheimer number $F_{\mathrm{r}} = \frac{F\varpi h x_1}{\nu}$, Drag force coefficient $F = \frac{C_{\mathrm{b}}}{\sqrt{K}}$, magnetic parameter $M = \frac{\sigma {B_0}^2 h^2}{\rho_{\mathrm{f}}\nu}$, Prandtl factor $P_{\mathrm{r}} = \frac{\nu}{\alpha'}$, Brownian coefficient $N_{\mathrm{b}} = \frac{\tau D_{\mathrm{B}}(C_0 - C_{\mathrm{h}})}{\alpha}$, thermophoresis coefficient $N_{\mathrm{t}} = \frac{\tau D_{\mathrm{T}}(T_0 - T_{\mathrm{h}})}{\alpha T_{\mathrm{h}}}$, Schmidt number $S_{\mathrm{c}} = \frac{\nu}{D_{\mathrm{B}}}$.

The skin friction coefficient C_{f} and the Nusselt number are defined as

$$C_{\mathrm{f}}^* = \left(\frac{Px_1}{h}\right)C_{\mathrm{f}} = f''(0),\ N_{\mathrm{u}_x} = \theta'(0)$$

, respectively.[36]

3 Solution methodology

This section is dedicated to the implementation of the shooting method to solve the transformed ordinary differential equations eqn (12)–(14) along with the boundary conditions eqn (15). One can easily observe that eqn (12) is independent of θ, so the solution of eqn (12) will be worked out first and then will be used as a known function in eqn (13) and (14). For this purpose, the following notations are used:

Denoting $f = \zeta_1, f' = \zeta_2, f'' = \zeta_3$ the resulting first order ODEs are:

The boundary conditions in eqn (15) have the following dimensionless form:

$$\left.\begin{array}{ll} \text{at } \eta = 0 & \zeta_1 = 0,\ \zeta_2 = 0,\ \zeta_3 = R,\ \zeta_4 = S,\ \zeta_5 = 0,\ \zeta_6 = 0, \\ & \zeta_7 = 1,\ \zeta_8 = 0,\ \zeta_9 = 0,\ \zeta_{10} = 0,\ \zeta_{11} = 0,\ \zeta_{12} = 1. \\ \text{at } \eta = 1 & \zeta_1 = 0,\ \zeta_2 = 0. \end{array}\right\} \tag{16}$$

$$\begin{aligned}
\zeta'_1 &= \zeta_2; & \zeta_1(0) &= 0, \\
\zeta'_2 &= \zeta_3; & \zeta_2(0) &= 0, \\
\zeta'_3 &= \zeta_4; & \zeta_3(0) &= R, \\
\zeta'_4 &= \left(\frac{\beta}{1+\beta}\right)P(\zeta_2\zeta_3 - \zeta_1\zeta_4) + \lambda\zeta_3 - 2\left(\frac{\beta}{1+\beta}\right) \\
&\quad F_{\mathrm{r}}\zeta_2\zeta_3 + M\left(\frac{\beta}{1+\beta}\right)\sin\gamma[\sin\gamma\zeta_3 - 2\delta\cos\gamma\zeta_2] = 0; & \zeta_4(0) &= S, \\
\zeta'_5 &= \zeta_6; & \zeta_5(0) &= 0, \\
\zeta'_6 &= \zeta_7; & \zeta_6(0) &= 0, \\
\zeta'_7 &= \zeta_8; & \zeta_7(0) &= 1, \\
\zeta'_8 &= \left(\frac{\beta}{1+\beta}\right)P(\zeta_3\zeta_6 + \zeta_2\zeta_7 - \zeta_4\zeta_5 - \zeta_1\zeta_8) + \lambda\zeta_7 - 2\left(\frac{\beta}{1+\beta}\right) \\
&\quad F_{\mathrm{r}}(\zeta_3\zeta_6 + \zeta_2\zeta_7) + M\left(\frac{\beta}{1+\beta}\right)\sin\gamma[\sin\gamma\zeta_7 - 2\delta\cos\gamma\zeta_6] = 0; & \zeta_8(0) &= 0, \\
\zeta'_9 &= \zeta_{10}; & \zeta_9(0) &= 0, \\
\zeta'_{10} &= \zeta_{11}; & \zeta_{10}(0) &= 0, \\
\zeta'_{11} &= \zeta_{12}; & \zeta_{11}(0) &= 0, \\
\zeta'_{12} &= \left(\frac{\beta}{1+\beta}\right)P(\zeta_3\zeta_{10} + \zeta_2\zeta_{11} - \zeta_4\zeta_9 - \zeta_1\zeta_{12}) + \lambda\zeta_{11} - 2\left(\frac{\beta}{1+\beta}\right) \\
&\quad F_{\mathrm{r}}(\zeta_3\zeta_{10} + \zeta_2\zeta_{11}) + M\left(\frac{\beta}{1+\beta}\right)\sin\gamma[\sin\gamma\zeta_{11} - 2\delta\cos\gamma\zeta_{10}] = 0; & \zeta_{12}(0) &= 1.
\end{aligned}$$

The Runge–Kutta method of order 4 solves the above system of 12 first-order differential equations with R and S missing initial conditions. These initial conditions are calculated by Newton's method, which is used to solve algebraic equations: $\zeta_1(\eta, R, S) = 0$ and $\zeta_2(\eta, R, S) = 0$. The following iterative formula is used for this purpose:

$$\begin{bmatrix} R^{n+1} \\ S^{n+1} \end{bmatrix} = \begin{bmatrix} R^{n} \\ S^{n} \end{bmatrix} - \begin{bmatrix} \zeta_5 & \zeta_9 \\ \zeta_6 & \zeta_{10} \end{bmatrix}_n^{-1} \begin{bmatrix} \zeta_1(1) - 0 \\ \zeta_2(1) - 0 \end{bmatrix}_n \quad (17)$$

The iterative process is repeated until the criterion listed below is met:

$$\max[|\zeta_1(\eta,R,S)|,|\zeta_2(\eta,R,S)|] < \varepsilon,$$

for an arbitrarily small positive value of ε. Throughout this work ε has been taken as 10^{-6}. Since eqn (13) and (14) are coupled equations they are solved separately by incorporating the solution of eqn (12) using the shooting technique. The method used in this study is advantageous over the existing numerical approaches in the literature: it first converts a boundary value problem into an initial value problem and then iteratively finds the missing initial conditions until the desired accuracy of the given boundary condition is reached. It is also applicable to a large number of associated problems in the literature in chemistry, physics and biology. In dealing with more complex problems it has to delineate numerical efficiency compared to other methods for related problems. Moreover, this numerical approach is also flexible and easy to implement through MATLAB and robust enough to deal with irregular boundary conditions within a boundary value problem. It is evidenced through numerical computations as seen in Table 1 and 2, that the presented numerical approach is highly accurate with appropriate refinement of the mesh, for solving boundary value problems. Table 1 and 2 show the accuracy of the obtained numerical solutions. The results of various physical parametric values are compared for the skin-friction coefficient and Nusselt number, with results obtained using the current method and through the built-in MATLAB function bvp4c. It is seen through Table 1 and 2 that the obtained numerical solutions are in strong agreement.

Table 1 Comparison of numerical values of $f''(0)$ (skin-friction coefficient)

F_r	M	N_b	λ	N_t	Present	bvp4c
0.1	1	0.1	0.2	0.1	3.5703852	3.5703849
1					2.8503317	2.8503313
2					2.0831872	2.0831865
	1				3.5703852	3.5703850
	3				3.5838796	3.5838789
	5				3.5907478	3.5907468
		0.1			3.5703852	3.5703842
		0.3			2.1543236	2.1543236
		0.5			2.0533960	2.0533954
			0.2		4.2755563	4.2755556
			0.4		4.2205923	4.2205911
			0.6		4.1918619	4.1918610
				0.1	3.5703852	3.5703844
				0.3	4.2635093	4.2635089
				0.5	4.9829068	4.9829059

Table 2 Comparison of numerical values of $\theta'(0)$ (Nusselt number)

F_r	M	N_b	λ	N_t	Present	bvp4c
0.1	1	0.1	0.2	0.1	1.5510276	1.5510262
1					1.5565799	1.5565783
2					1.5623997	1.5623989
	1				1.5510276	1.5510271
	3				0.7990043	0.7990039
	5				0.4052419	0.4052411
		0.1			1.5510276	1.5510271
		0.3			0.9392732	0.9392729
		0.5			0.8955695	0.8955689
			0.2		1.5416834	1.5416831
			0.4		1.5419289	1.5419278
			0.6		1.5420601	1.5420599
				0.1	1.5510276	1.5510267
				0.3	1.8665458	1.8665445
				0.5	2.1915619	2.1915618

4 Representation of graphs

This section is dedicated to providing the physical reasoning for the three essential profiles – speed, temperature, and nanoparticle concentration – through graphs. Fig. 2–20 are sketched to expose the consequences of several fluid parameters disconcerted in the flow model.

Fig. 2 and 3 are pictorial descriptions of f and f' with changing Forchheimer number, respectively. A closer view highlights that the velocity region decreases with an increase in the Forchheimer number. The relation of the Forchheimer number with the skin friction coefficient is accountable for this trend in the velocity parameter. An exhaustive range is available for increasing Forchheimer number; hence, the drag stress constant produces more friction supplied to the fluid flow, which leads to a decline in the velocity profile.

Fig. 4 and 5 indicate the influence of the magnetic parameter on fluid flow within a Darcy medium. An inverse relationship between the fluid flow and the magnetic number can be seen. A

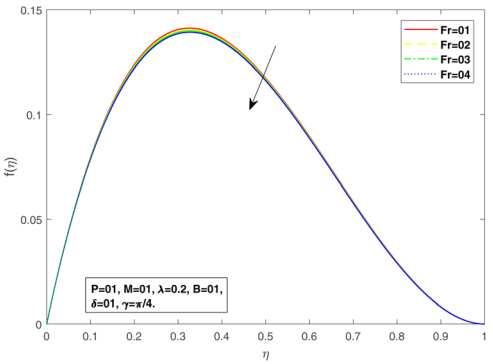

Fig. 2 Consequences of F_r on $f(\eta)$.

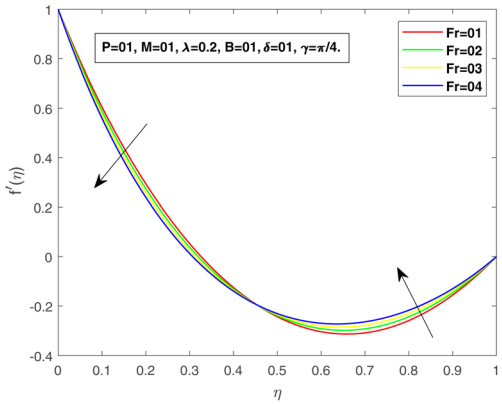

Fig. 3 Consequences of F_r on $f'(\eta)$.

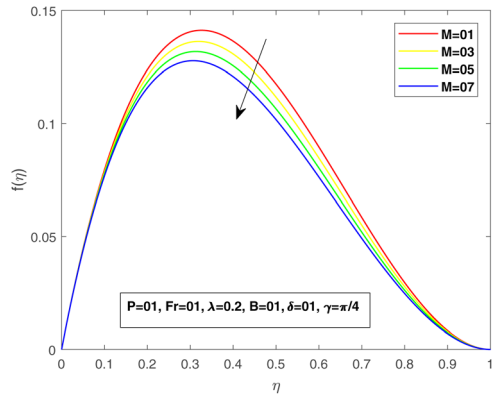

Fig. 4 $f(\eta)$ for increasing M.

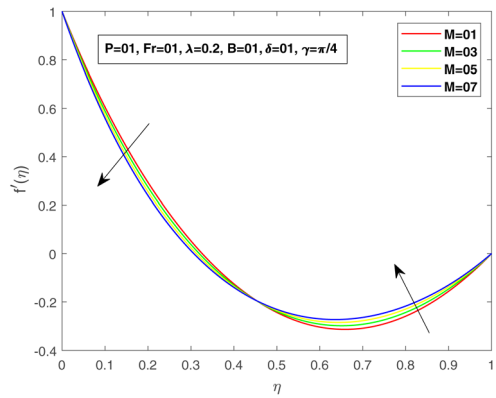

Fig. 5 $f'(\eta)$ for increasing M.

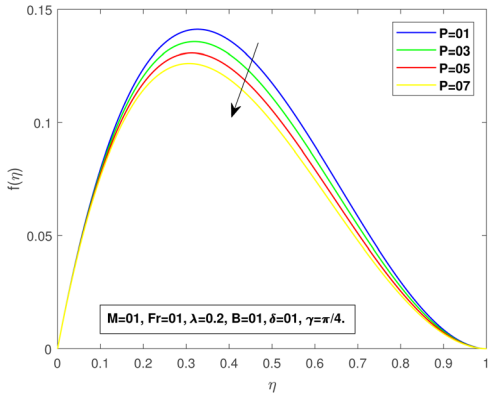

Fig. 6 $f(\eta)$ for increasing values of P.

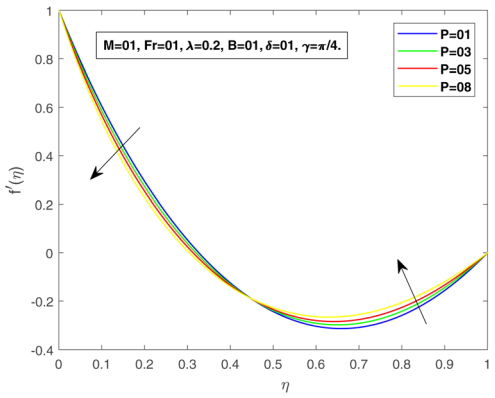

Fig. 7 $f'(\eta)$ for increasing values of P.

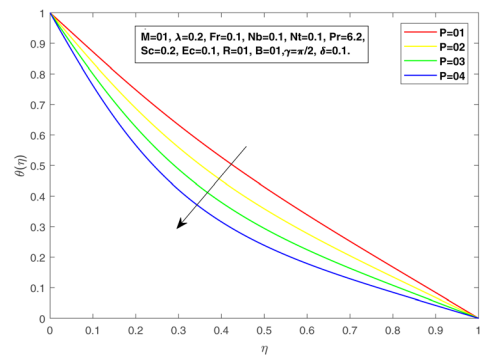

Fig. 8 $\theta(\eta)$ for increasing values of P.

magnetic region acting at an angle γ to the surface produces certain collisions towards the fluid flow; therefore, a decrease is evidenced in each f and f'. The viscosity parameter P, impact on f and f' is shown in Fig. 6 and 7. Physically, for bigger values of P, a decrease in the kinematic viscosity assures an increase in the dynamic viscosity, and consequently, a reduction in the velocity profile is observed.

Fig. 8 suggests the impact of the viscosity constant on the temperature profile. The thermal boundary layer is reduced for increasing values of the viscosity constant. The effect of diffusive Brownian motion on the temperature distribution is shown in Fig. 9, while Fig. 10 is presented to reflect the impact of thermophoresis on the temperature distribution. The rapid and random movement of nanoparticles due to the Brownian motion raises the thermophoretic pressure, resulting in speedy fluid motion from the warm region to a lower temperature region. Therefore, an upward thrust in temperature distribution is discovered for each parameter. For multiplied values of the viscosity coefficient, we may see an augmentation in the

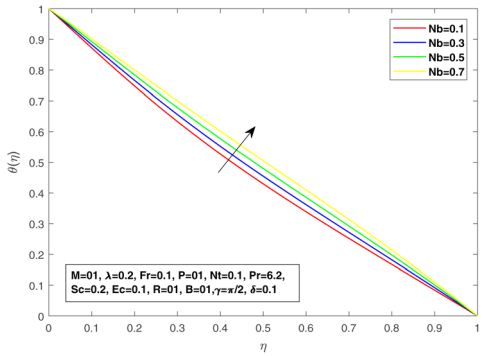

Fig. 9 $\theta(\eta)$ for increasing values of N_b.

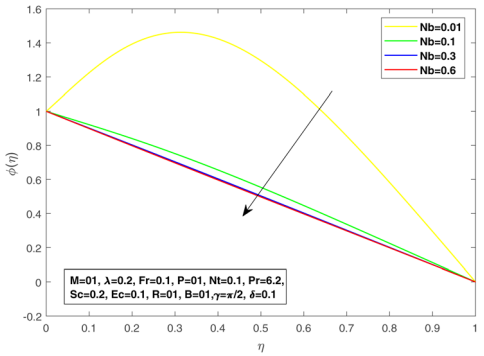

Fig. 12 $\phi(\eta)$ for increasing values of N_b.

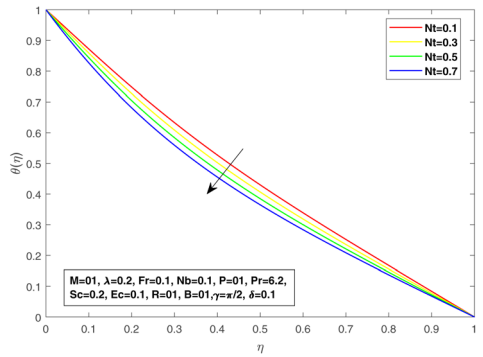

Fig. 10 $\theta(\eta)$ for increasing values of N_t.

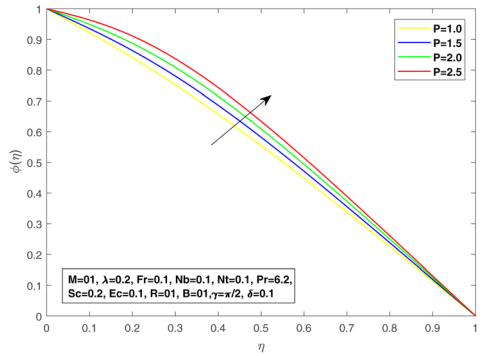

Fig. 11 $\phi(\eta)$ for increasing values of P.

concentration profile as proven in Fig. 11, which authorizes the mathematical formulation and physical significance of the viscosity parameter in the fluid flow. The concentration profile is reduced with increasing values of the Brownian diffusive movement parameter. The random movement reduces with enhanced Brownian motion, but the case is contrary to that of thermophoresis. At $N_b = 0.01$, an obvious effect of Brownian diffusion can be seen, but the impact is minimal with further increments in N_b. In addition, a linear increase is visible in the concentration profile with an improvement in N_t. Fig. 12 and 13 are plotted by taking N_u as a function of the viscosity parameter P for different values of Brownian diffusion parameter N_b and thermophoresis N_t, respectively. It can be seen in Fig. 14 that with an increase in P, N_u increases; and for a fixed value of P with increasing N_t, a decline in N_u can be seen. The same behavior can be seen in Fig. 15 for values of N_b.

Fig. 16 and 17 are sketched to estimate the variation in skin friction as a function of the viscosity parameter by changing the values of λ and M, respectively. The larger friction is produced with the useful resource of Forchheimer medium and retardation provided through magnetic effect results in skin-friction enhancement. The effect of the Prandtl constant on the thermal boundary layer is demonstrated in Fig. 18 shows a decline in temperature profile for large values of Pr.

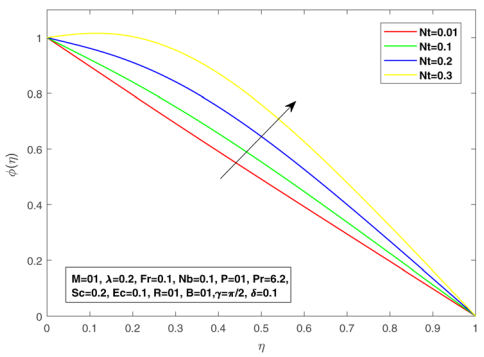

Fig. 13 $\phi(\eta)$ for increasing values of N_t.

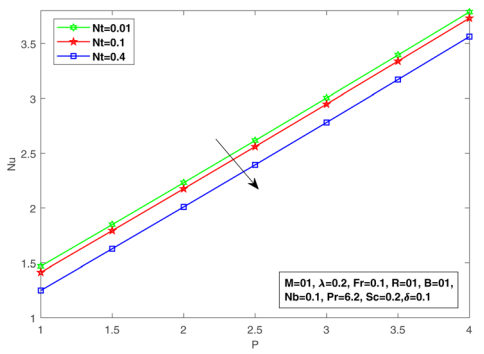

Fig. 14 Nusselt number w. r. t P and N_t.

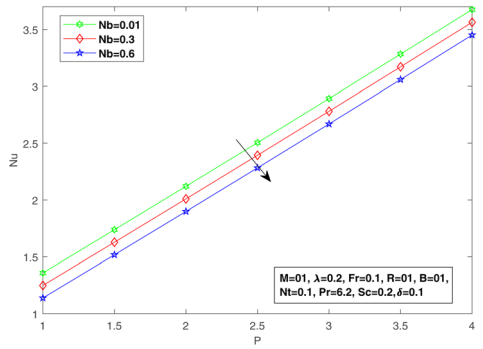

Fig. 15 Nusselt number w. r. t P and N_b.

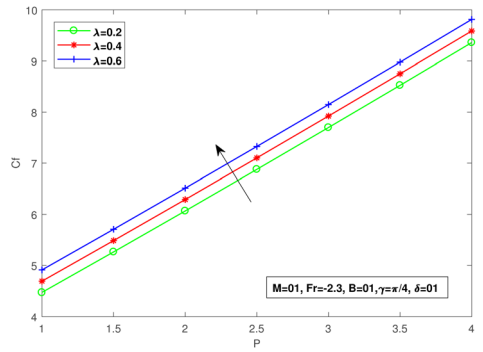

Fig. 16 Skin friction for porosity factor λ.

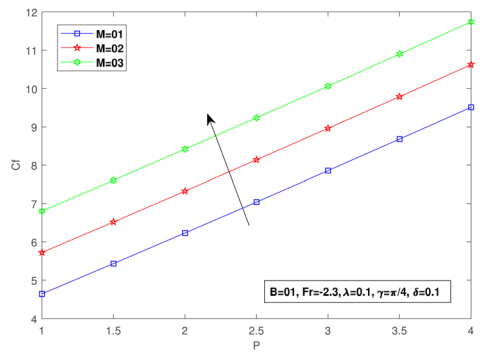

Fig. 17 Skin friction for magnetic parameter M.

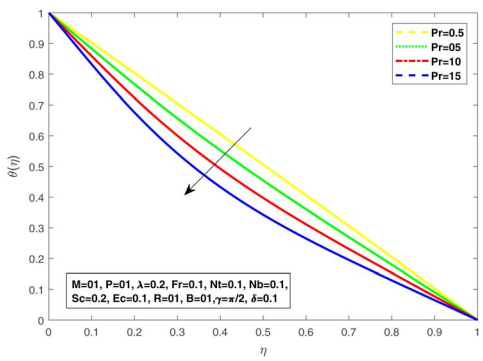

Fig. 18 $\theta(\eta)$ for various values of Pr.

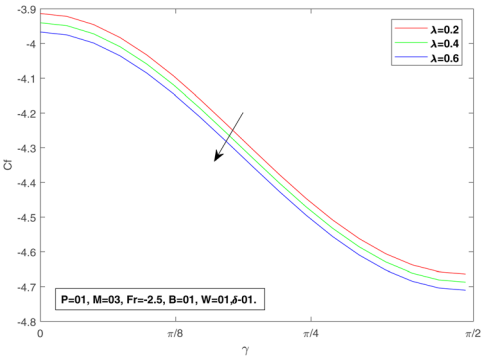

Fig. 19 Skin friction w. r. t γ and λ.

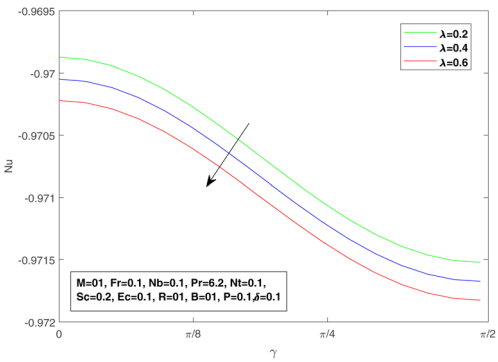

Fig. 20 Nusselt number w. r. t γ and λ.

Fig. 19 is a plot of the skin friction as a function of inclination angle γ with changing porosity factor λ. We can see a decrease in C_f by increasing the value of λ. Fig. 20 is delineated to demonstrate the Nusselt number as a function of the angle of inclination γ by changing porosity factor λ values. We can see a decrease in the Nusselt number with increasing the value of λ.

5 Concluding remarks

In this article, the work of Rasool *et al.*[36] is extended to the effect of the inclined magnetic field, Casson fluid, viscous dissipation, Brownian motion, thermophoresis diffusion, and chemical reaction. First, governing equations of the physical problem are transformed into ODEs *via* similarity transformations. Numerical solutions have been determined for the converted boundary value problem by incorporating the shooting technique. The numerical consequences are provided as graphs for temperature, momentum, and concentration profiles using various values of the governing physical parameters. The achievements of contemporary studies can be summarized below:

- Velocity decreases for a large Forchheimer constant. The skin friction coefficient is responsible for such behavior.
- The effect of a magnetic parameter is reversely associated with the flow velocity. The depth of the momentum boundary layer is reduced.
- For increasing values of the viscosity parameter, a reduction in the velocity field is observed due to the inverse relation of kinematic viscosity with dynamic viscosity.

• The random motion of nanoparticles increases due to Brownian diffusion. This is because a stronger thermophoretic force ensures speedy transport from the warm region to the cold region.

• Augmentation in the concentration profile is observed for larger values of the viscosity parameter.

• The heat flux rate diminishes for diffusive Brownian motion and thermophoresis.

• The surface drag force is increased for accelerated porosity and magnetic parameters.

• For increasing porosity factor (λ) and the angle of magnetic inclination (γ), the skin friction (C_f) decreases and the Nusselt number (N_u) decreases. Moreover, skin friction and Nusselt number are decreasing functions with angle of inclination.

As an overall outlook, future studies can address the aforementioned problem by taking ion slip and Hall effects into consideration, see for instance ref. 39.

Nomenclature

B_0	Magnetic number [—]
C	Concentration of nanoparticles [mol m^{-3}]
$(c_p)_f$	Specific heat of fluid [M L^2 T^{-2} K^{-1}]
D_B	BDC [—]
D_T	TDC [—]
E_c	Eckert number [—]
f, h	Dimensionless velocity components [—]
K_c	Constant rate of chemical reaction [—]
M	Dimensionless magnetic parameter [—]
ρ	Density [ML^{-3}]
N_b	Dimensionless BDC [—]
N_t	Dimensionless TDC [—]
N_u	Nusselt number [—]
P	Viscosity constant [—]
R	Thermal radiation parameter [—]
P_r	Prandtl number [—]
S_c	Schmidt number [—]
u_1, u_2	Velocity components [ms^{-1}]
C_f	Skin friction [—]
T	Temperature [K]
α	Thermal diffusivity of nanofluid [m^2 s^{-1}]
β	Casson fluid parameter [—]
γ	Chemical reaction parameter [—]
k	Thermal conductivity [W m^{-1} K^{-1}]
δ	Heat generation/absorption [—]
ν	Kinematic viscosity [M L^2 T^{-1}]
μ	Dynamic viscosity [M L^2 T^{-1}]
ϕ	Nanoparticle volume fraction [—]
η	Similarity variable [—]
θ	Dimensionless temperature [—]
τ	Ratio of heat capacity [—]
x_1, x_2	Cartesian coordinates [—]

Conflicts of interest

There are no conflicts to declare.

References

1 A. J. Chamkha, MHD-free convection from a vertical plate embedded in a thermally stratified porous medium with Hall effects, *Appl. Math. Modell.*, 1997, **21**(10), 603–609.
2 A. J. Chamkha, Non-Darcy hydromagnetic free convection from a cone and a wedge in porous media, *Int. Commun. Heat Mass Transfer*, 1996, **23**(6), 875–887.
3 M. V. Krishna, N. A. Ahammad and A. J. Chamkha, Radiative MHD flow of Casson hybrid nanofluid over an infinite exponentially accelerated vertical porous surface, *Case Stud. Therm. Eng.*, 2021, **27**, 101229.
4 M. Keimanesh, M. M. Rashidi, A. J. Chamkha and R. Jafari, Study of a third grade non-Newtonian fluid flow between two parallel plates using the multi-step differential transform method, *Comput. Math. Appl.*, 2011, **62**(8), 2871–2891.
5 A. J. Chamkha, T. Groşan and I. Pop, Fully developed free convection of a micropolar fluid in a vertical channel, *Int. Commun. Heat Mass Transfer*, 2002, **29**(8), 1119–1127.
6 M. Stefan, Versuchuber die scheinbare adhäsion, sitzungsber, *Abt. II, Österr. Akad. Wiss. Math.-Naturwiss. Kl*, 1874, vol. 69, pp. 713–721.
7 M. M. Rashidi, H. Shahmohamadi and S. Dinarvand, Analytic approximate solutions for unsteady two-dimensional and axisymmetric squeezing flows between parallel plates, *Math. Probl. Eng.*, 2008, **2008**, 935095.
8 T. Hayat, A. Qayyum and A. Alsaedi, Three-dimensional mixed convection squeezing flow, *Appl. Math. Mech.*, 2015, **36**(1), 47–60.
9 T. Hayat, T. Muhammad, A. Qayyum, A. Alsaedi and M. Mustafa, On squeezing flow of nanofluid in the presence of magnetic field effects, *J. Mol. Liq.*, 2016, **213**, 179–185.
10 H. Shahmohamadi and M. M. Rashidi, Vim solution of squeezing MHD nanofluid flow in a rotating channel with lower stretching porous surface, *Adv. Powder Technol.*, 2016, **27**(1), 171–178.
11 S. Murtaza, P. Kumam, Z. Ahmad, M. Ramzan, I. Ali and A. Saeed, Computational Simulation of Unsteady Squeezing Hybrid Nanofluid Flow Through a Horizontal Channel Comprised of Metallic Nanoparticles, *J. Nanofluids*, 2023, **12**(5), 1327–1334.
12 A. Rostami, K. Hosseinzadeh, and D. Ganji, Hydrothermal analysis of ethylene glycol nanofluid in a porous enclosure with complex snowflake shaped inner wall, *Waves in Random and Complex Media*, 2022, vol. 32, issue 1, pp. 1–18.
13 Z. Shah, M. Sheikholeslami, P. Kumam, et al., Influence of nanoparticles inclusion into water on convective magneto hydrodynamic flow with heat transfer and entropy generation through permeable domain, *Case Stud. Therm. Eng.*, 2020, **21**, 100732.
14 S. Murtaza, P. Kumam, Z. Ahmad, K. Sitthithakerngkiet, and T. Sutthibutpong, Fractional Model of Brinkman-Type Nanofluid Flow with Fractional Order Fourier's and Fick's Laws, Fractals, 2023.

15 S. Murtaza, P. Kumam, M. Bilal, T. Sutthibutpong, N. Rujisamphan and Z. Ahmad, Parametric simulation of hybrid nanofluid flow consisting of cobalt ferrite nanoparticles with second-order slip and variable viscosity over an extending surface, *Nanotechnol. Rev.*, 2023, **12**(1), 20220533.

16 S. Murtaza, P. Kumam, Z. Ahmad, T. Seangwattana and I. E. Ali, Numerical analysis of newly developed fractal-fractional model of Casson fluid with exponential memory, *Fractals*, 2022, **30**(05), 2240151.

17 M. S. Khan and T. Dil, Heat transfer enhancement of automobile radiator using h_2o–cuo nanofluid, *AIP Adv.*, 2017, **7**(4), 045018.

18 S. U. Choi and J. A. Eastman, Enhancing thermal conductivity of fluids with nanoparticles, *Tech. Rep.*, Argonne National Lab.(ANL), Argonne, IL (United States), 1995.

19 S. Parvin and A. Chamkha, An analysis on free convection flow, heat transfer and entropy generation in an odd-shaped cavity filled with nanofluid, *Int. Commun. Heat Mass Transfer*, 2014, **54**, 8–17.

20 A. Zaraki, M. Ghalambaz, A. J. Chamkha, M. Ghalambaz and D. De Rossi, Theoretical analysis of natural convection boundary layer heat and mass transfer of nanofluids: effects of size, shape and type of nanoparticles, type of base fluid and working temperature, *Adv. Powder Technol.*, 2015, **26**(3), 935–946.

21 P. S. Reddy and A. J. Chamkha, Soret and dufour effects on MHD convective flow of Al2O3–water and TiO2–water nanofluids past a stretching sheet in porous media with heat generation/absorption, *Adv. Powder Technol.*, 2016, **27**(4), 1207–1218.

22 A. Chamkha, M. Ismael, A. Kasaeipoor and T. Armaghani, Entropy generation and natural convection of CuO-water nanofluid in C-shaped cavity under magnetic field, *Entropy*, 2016, **18**(2), 50.

23 G. Rasool, A. Shafiq, C. M. Khalique and T. Zhang, Magnetohydrodynamic Darcy–Forchheimer nanofluid flow over a nonlinear stretching sheet, *Phys. Scr.*, 2019, **94**(10), 105221.

24 M. A. Ismael, T. Armaghani and A. J. Chamkha, Conjugate heat transfer and entropy generation in a cavity filled with a nanofluid-saturated porous media and heated by a triangular solid, *J. Taiwan Inst. Chem. Eng.*, 2016, **59**, 138–151.

25 M. Sohail and R. Naz, Modified heat and mass transmission models in the magnetohydrodynamic flow of sutterby nanofluid in stretching cylinder, *Phys. A*, 2020, **549**, 124088.

26 I. Tlili, W. Khan and K. Ramadan, MHD flow of nanofluid flow across horizontal circular cylinder: steady forced convection, *J. Nanofluids*, 2019, **8**(1), 179–186.

27 A. Wakif, Z. Boulahia, A. Amine, I. Animasaun, M. Afridi, M. Qasimd and R. Sehaqui, Magneto-convection of alumina-water nanofluid within thin horizontal layers using the revised generalized buongiorno's model, *Front. Heat Mass Transfer*, 2019, **12**, 1–15.

28 K. Hosseinzadeh, A. Mogharrebi, A. Asadi, M. Sheikhshahrokhdehkordi, S. Mousavisani and D. Ganji, Entropy generation analysis of mixture nanofluid (H2O/c2H6O2)–Fe3O4 flow between two stretching rotating disks under the effect of MHD and nonlinear thermal radiation, *Int. J. Ambient Energy*, 2022, **43**(1), 1045–1057.

29 Z. Shah, M. R. Hajizadeh, N. A. Alreshidi, W. Deebani, M. Shutaywi, et al., Entropy optimization and heat transfer modeling for lorentz forces effect on solidification of NEPCM, *Int. Commun. Heat Mass Transfer*, 2020, **117**, 104715.

30 M. S. Khan and T. Dil, Numerical computation of heat transfer enhancement through cosserat hybrid nanofluids using continuous galerkin–petrov method, *Eur. Phys. J. Plus*, 2020, **135**(2), 1–19.

31 P. Forchheimer, Wasserbewegung durch boden, *Z. Ver. Deutsch Ing.*, 1901, **45**, 1782–1788.

32 M. Muskat and R. Wyckoff, *The Flow of Homogeneous Fluids through Porous Media*, JW Edwards, Ann Arbor, Michigan, 1937.

33 M. Seddeek, Influence of viscous dissipation and thermophoresis on darcy–forchheimer mixed convection in a fluid saturated porous media, *J. Colloid Interface Sci.*, 2006, **293**(1), 137–142.

34 M. A. Sadiq and T. Hayat, Darcy–forchheimer flow of magneto maxwell liquid bounded by convectively heated sheet, *Results Phys.*, 2016, **6**, 884–890.

35 T. Hayat, F. Shah, M. I. Khan and A. Alsaedi, Framing the performance of heat absorption/generation and thermal radiation in chemically reactive darcy-forchheimer flow, *Results Phys.*, 2017, **7**, 3390–3395.

36 G. Rasool, W. A. Khan, S. M. Bilal and I. Khan, MHD squeezed Darcy–Forchheimer nanofluid flow between two h–distance apart horizontal plates, *Open Phys.*, 2020, **18**(1), 1100–1107.

37 J. Buongiorno, *Convective Transport in Nanofluids*, 2006.

38 M. Sheikholeslami, M. Rashidi, D. M. Al Saad, F. Firouzi, H. B. Rokni and G. Domairry, Steady nanofluid flow between parallel plates considering thermophoresis and brownian effects, *J. King Saud Univ., Sci.*, 2016, **28**(4), 380–389.

39 M. V. Krishna, B. Swarnalathamma and A. J. Chamkha, Investigations of Soret, Joule and Hall effects on MHD rotating mixed convective flow past an infinite vertical porous plate, *J. Ocean Eng. Sci.*, 2019, **4**(3), 263–275.